PROCEEDINGS A

rspa.royalsocietypublishing.org

Research

Cite this article: Kothari M, Cha M-H, Kim K-S. 2018 Critical curvature localization in graphene. I. Quantum-flexoelectricity effect. *Proc. R. Soc. A* **474**: 20180054.
http://dx.doi.org/10.1098/rspa.2018.0054

Received: 29 January 2018
Accepted: 18 May 2018

Subject Areas:
mechanics, nanotechnology, atomic and molecular physics

Keywords:
critical hinge-mode buckling, multi-layer graphene, graphene corrugation, curvature localization, quantum flexoelectricity, flexoelectric crinkle

Author for correspondence:
Kyung-Suk Kim
e-mail: kyung-suk_kim@brown.edu

Critical curvature localization in graphene. I. Quantum-flexoelectricity effect

Mrityunjay Kothari, Moon-Hyun Cha and Kyung-Suk Kim

School of Engineering, Brown University, Providence, RI 02912, USA

K-SK, 0000-0003-0681-346X

Here, we report the discovery of a new, curvature-localizing, subcritical buckling mode that produces shallow-kink corrugation in multi-layer graphene. Our density functional theory (DFT) analysis reveals the mode configuration—an approximately 2 nm wide boundary layer of highly localized curvature that connects two regions of uniformly but oppositely sheared stacks of flat atomic sheets. The kink angle between the two regions is limited to a few degrees, ensuring elastic deformation. By contrast, a purely mechanical model of sandwich structures shows progressive supercritical curvature localization spread over a 50–100 nm wide boundary layer. Our effective-locality model of electromechanics reveals that coupling between atomic-layer curvature and electric-charge polarization, i.e. quantum flexoelectricity, leads to emergence of a boundary layer in which curvature is focused primarily within a 0.86 nm fixed band width. Both DFT and the model analyses show focused distributions of curvature and polarization exhibiting oscillating decay within the approximately 2 nm wide boundary layer. The results show that dipole–dipole interaction lowers the potential energy with such a distribution. Furthermore, this model predicts peak-polarization density approximately 0.12 $e^{-}\,nm^{-1}$ for 3° tilt angle. This high polarization concentration can be controlled by macroscopic deformation and is expected to be useful in studies of selective graphene-surface functionalization for various applications.

THE ROYAL SOCIETY PUBLISHING

1. Introduction

In this paper, we report discovery of peculiar curvature localization in graphene at the nanoscale, that produces unprecedented class of surface corrugation—the *quantum flexoelectric crinkle*. To this end, we begin with reviewing historical observations and current understanding of graphene corrugation. Recently, it has been reported that single-layer graphene (SLG) and few-layer graphene (FLG) exhibit characteristic *dynamic* ripples as well as *static* corrugations when suspended [1,2]. Regarding the dynamic ripples, Meyer *et al*. [1] studied dynamic morphologies of suspended SLG sheets, analysing broadening of transmission electron microscope (TEM) electron beam diffraction, and concluded that suspended SLG sheets are not perfectly flat. Instead, the sheets ripple with a prevailing wavelength (≤ 25 nm) at a frequency of tens of GHz [1,2]. They explained that the characteristic rippling is caused by two competing mechanisms. One is thermally excited diverging amplitude of long-wavelength ripples that would lead to crumpling [3–5], and the other is a coupling between bending and stretching in 2D rippling that stabilizes the layer against crumpling [6]. In addition to dynamic rippling, the time-average configuration of fluctuating ripples, i.e. the static configuration, of a suspended FLG is not flat either. Meyer *et al*. [1] also presented a real-space TEM static image of FLG hexagonal-lattices, the visibility of which strongly depended on their tilt angle. The FLG image showed static corrugation with characteristic size somewhat smaller than the characteristic SLG ripple size. Regarding corrugation of general multi-layer graphene (MLG) or graphite, Ohler *et al*. [7] reported an X-ray diffraction topographic study of highly oriented pyrolytic graphite (HOPG). This showed crystallographic X-ray peak spreading of the Cu-Kα rocking curve, which represents 'mosaic spread'—a non-uniformity measure of atomic-layer parallelism. The mosaic spread of MLG corresponds to discrete tilt-angle variation, up to $\pm 3.5°$, among zones of flat atomic layers that range from tens of nanometres to a few microns, in contrast to smooth wrinkles of SLG [8].

From the prior observational results, two major questions arise; what are the conditions of elastostatic graphene deformation to yield smooth ripples versus corrugated flat-zone segments? And, are there lower-energy modes than the harmonic modes? To answer these questions, we start with a benchmark experiment. Figure 1*a* and *b* show schematics of the suspended-MLG buckling in the experiment. At first, we consider a bilayer graphene to understand major mechanisms of the MLG buckling. We model the bilayer with weak van der Waals interlayer coupling as a sandwich structure to determine the purely mechanical behaviour without electromechanical coupling. Elastic buckling of sandwich structures has been well studied [9,10], and Hunt *et al*. [10] reported analysis of interactive buckling in sandwich structures among three different eigen modes of bilayer buckling—*snake*, *hour-glass* and *overall-bending* modes. In this paper, we will call the shear-snake mode as interlayer-shear mode, ignoring the tilt-snake mode [10], because MLG has an extreme stiffness ratio (approx. 250) of the intralayer tension to the interlayer shear. In addition, we find in this paper that the interlayer-shear mode of deformation prevails over the overall-bending mode in buckling at the nanoscale, unless the structure is extremely slender. If the sandwich-structure model is employed, the interlayer-shear-mode buckling is expected to progressively develop a kink configuration as the amplitude grows. The interlayer-shear-mode evolves from a sinusoidal profile to a symmetric kink-like shape with the ends nearly straight as shown in figure 1*b*. However, in our experiment, an MLG directly, i.e. not progressively, buckles out of plane into a *hinge mode*, i.e. the shallow symmetric kink shape, as shown in figure 1*c*. In the experiment, the assembly of MLG (approx. 200 layers) attached to PMMA grating of 1-µm grooves is compressed up to approximately 0.1% strain to observe the buckling mode of the suspended MLG with an atomic force microscope (AFM). This remains below the critical symmetric kink angle of 6°–7° required for the MLG to emit interlayer-sliding van der Waals dislocations from the kink ridge [11], and deform inelastically.

The overall-bending mode, also known as Euler bending mode [12], grows in amplitude from an infinitesimal sinusoidal profile of pitchfork bifurcation, progressively to a smooth post-buckling wrinkle configuration in a supercritical state [13–15]. When a soft-core sandwich structure attached to a soft substrate or periodically suspended on an elastic substrate is

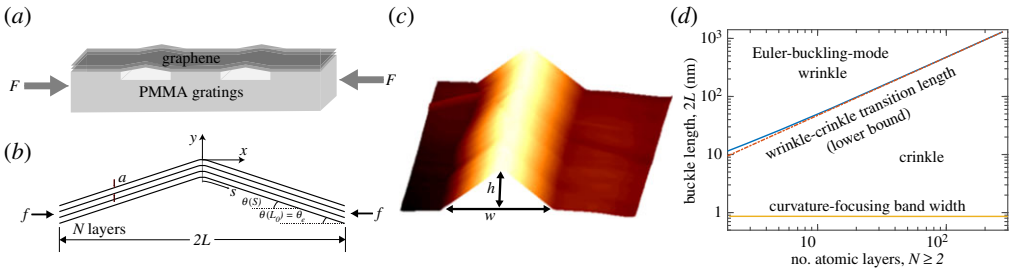

Figure 1. (*a*) A schematic of MLG attached to PMMA gratings, buckling under the compressive lateral load *F*; (*b*) Geometry of buckled N-layered MLG crinkle with end-angle θ_e (The layers are parallel and characterized by angle $\theta(s)$ made with the horizontal, with *s* being the arclength.); (*c*) Atomic force microscopy (AFM) image of MLG crinkle with $h = 88$ nm and $w = 1\,\mu$m; (*d*) Buckling phase map identifying regions of wrinkle mode and crinkle mode for N-layered MLG of length $2L_0$ (curvature-focusing band width for flexoelectric crinkle approximately 0.86 nm is marked by the yellow line.). (Online version in colour.)

compressed, the structure buckles periodically in an interlayer-shear mode. The interlayer-shear mode of purely mechanical buckling also supercritically develops its post-buckling configuration from an infinitesimal sinusoidal bifurcation profile [9,10]. The post-buckling configuration progressively evolves into a series of periodic kinks which we term 'crinkle ruga' or simply 'crinkles' [16]. Here, we collectively denote all corrugation geometries such as wrinkles, creases, ridges, folds, crumples and crinkles as 'rugae' [17–20]. Figure 1*d* shows a map of wrinkle versus crinkle formation depending on the slenderness of the MLG (see appendix A for the analysis). If the film is extremely slender, i.e. the length is beyond a critical value for a given number of atomic layers, the MLG develops wrinkles in the overall-bending mode under axial compression. Otherwise, the MLG develops crinkles. The crinkle, if mechanically modelled as an interlayer-shear mode, supercritically and progressively focuses its curvature within an evolving band width (EBW). By contrast, we find in this paper that if the effects of intralayer as well as interlayer long-range flexoelectric interactions are taken into account, the MLG subcritically buckles into a hinge mode at the onset of buckling, focusing the curvature within a fixed band width (FBW). Then, the mode shape remains invariant while the amplitude grows. The FBW is depicted as a horizontal line near the bottom in figure 1*d*. The FBW thickness is obtained by *ab initio* calculations based on quantum density functional theory (DFT) in the following section, and the criticality of the flexoelectric crinkle formation is analysed in subsequent sections.

Among the critical bifurcations in buckling of sandwich structures, hour-glass mode of buckling, if excited, would undergo subcritical bifurcation [10]. However, the post-buckling equilibrium configuration of the hour-glass mode is a relatively high-energy state requiring substantial axial loading [10]. From the energetics point of view, the potential energy of the deformed graphene at the nanoscale can be significantly varied through long-range nonlocal electrostatic interactions among flexoelectric dipoles, besides local strain energy variations. Graphene is an electrostatically centrosymmetric crystal, and MLG cannot be polarized by affine deformation, i.e. not piezoelectric. However, symmetry-breaking deformation, i.e. strain gradients, can polarize graphene by shifting the spatial distribution of the quantum states of electrons, making the graphene flexoelectric [21–23]. Since graphene is an in-plane conductor at a finite temperature and sustains static polarization only in the direction normal to the lattice layer, graphene is statically both dielectric and flexoelectric, in the normal direction. The static polarization is proportional to the normal component of the point-exclusive external electric field [24] and the local curvature of the layer. The dielectric constant was evaluated by DFT for SLG in [25] and FLG in [26], and the overall polarization induced by uniform curvature was provided for SLG in [27], also by DFT. Since dipole–dipole interaction energy is sensitive to both the interaction directions and the orientations of the polarizations, in this paper, we are interested in determining

which flexoelectric mechanisms create the experimentally observed subcritical hinge mode of crinkle in MLG buckling.

2. Multiphysics buckling models of multi-layer graphene

In this section, we first analyse details of the energetics and stable mode shapes of graphene buckling with DFT for a relatively short, 13.2619 nm, span. Then, the results are compared with purely mechanical and electro-mechanical coupling models of MLG crinkles.

(a) Density functional theory analysis of graphene crinkles

We investigate formation and stability of crinkle structures of 1–3 layers of graphene and bulk graphite using DFT calculations, employing the Vienna *ab initio* simulation package (VASP) [28] with the projector augmented wave pseudo-potential [29]. Exchange correlation interactions are treated within the local density approximation. The energy cutoff for the plane-wave basis set is set to 375 eV throughout the whole calculation, and a k-point grid of $1 \times 12 \times 1$ is used for the layered graphene supercell of $13.2619 \times 0.426\,\text{nm}^3$ with periodic boundary conditions. A grid of $1 \times 12 \times 12$ k-points is used for the bulk graphite totalling a volume of $13.2619 \times 0.426 \times 0.68\,\text{nm}^3$. Periodic boundary conditions are used and we set more than 1.5 nm vacuum in z-direction to avoid artificial interaction between layers in different supercell repeated in z-direction. Using the plane-wave-based total energy minimization [30], the structures were relaxed until the force on each atom was less than $0.01\,\text{eV}\,\text{Å}^{-1}$.

Figure 2*a* shows the top view of the simulation supercell. The end displacements of the MLG were constrained but kept free to rotate by setting the lateral (x-direction) length of the supercell close to the value corresponding to the crinkle angle of interest. Then, the structure was fully relaxed to the minimum energy configuration through iterative DFT calculations. Figure 2*b* shows the post-buckling morphology which compares favourably to the experimentally observed crinkle configuration (figure 1*c*). This configuration exhibits a distinct crinkle mode which is slightly sensitive to the bending direction, depending on whether it is along armchair or zigzag orientations as seen in the figure 2*c*. For the bulk simulation, the translational symmetry is enforced along the thickness direction to make all the layers deform identically. The curvature as a function of position is given in figure 2*d*. The curvature is localized within a boundary layer of approximately 2 nm width around the centre and vanishes everywhere else. In the boundary layer, the curvature is highly concentrated or focused within a band width defined by the two symmetric inflection points of the curvature distribution closest to the centre. The band width of curvature focusing, approximately 0.86 nm, is nearly invariant with respect to variations of the crinkle end angle. The curvature is focused within the FBW even at a very small kink angle, e.g. 0.1°. The curvature distribution scaled only by the end angle in the FBW implies that the post-buckling mode of the MLG crinkle is invariant for different end angles. This is in stark contrast to the Euler buckling mode or the mechanical interlayer-shear mode for which the curvature is broadly distributed over the length of the graphene layers, and the distribution evolves progressively as a function of the end angle. Another important feature of the MLG crinkle configuration is the curvature reversal observed immediately outside of the curvature focusing band, which is not observed in purely mechanical models of sandwich structures.

We also carried out the calculation with various initial configurations to search for possible locally stable configurations (i.e. local minima of the total energy). The result shows that the sine-wave configuration with the period of the supercell length is also a local energy-minimum configuration. The sinusoidal wrinkle configuration is more stable than the crinkle configuration for SLG. Surprisingly, the crinkle configuration is also locally stable in SLG for the supercell span; the stabilizing mechanism is revealed to be flexoelectric dipole–dipole interactions in following sections. The local energy-minimum characteristics of SLG crinkle is likely an important aspect of understanding possible dynamic hopping in SLG ripples. For two or more layers of graphene including graphite, however, the crinkle configuration is more stable than the

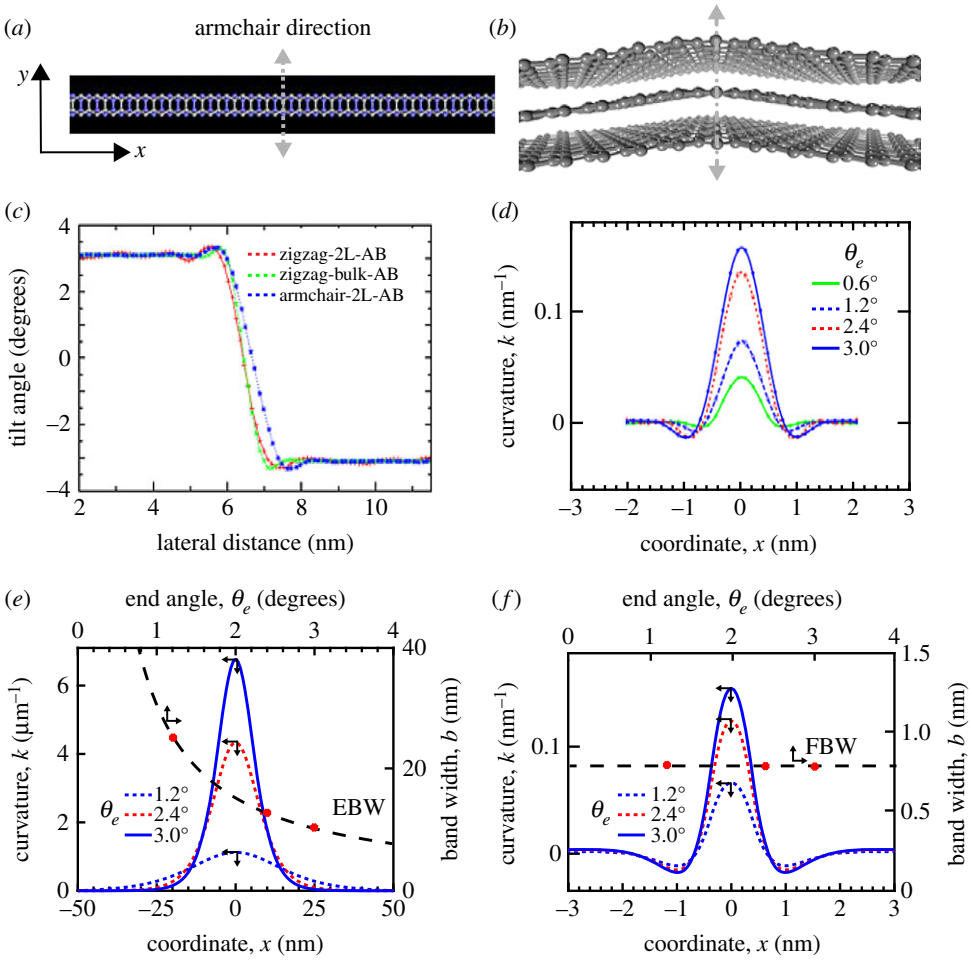

Figure 2. DFT analysis (*a–b*): (*a*) Top view of simulation supercell for MLG; (*b*) side view of buckled MLG—the crinkle mode; (*c*) Crinkle slope profile, $\theta(x)$, for different configurations, showing the zones of flat atomic layers; (*d*) curvature distribution for different end angles, showing the localization in an approximately 2 nm width around the centre. *Nanostructure modelling* (*e*,*f*): (*e*) curvature distribution versus position (left and bottom axes), and EBW versus end angle (right and top axes) from the purely mechanical model for 21-layered, 100 nm long MLG; (*f*) curvature distribution versus position (left and bottom axes), and FBW versus end angle (right and top axes) from the e-local flexoelectric model for 21-layered, 15 nm long MLG. (Online version in colour.)

sine-wave. Searching from various trial initial configurations, we could not find any other configuration that is more stable than crinkle under the given boundary condition, which implies that the crinkle is potentially in static ground state of MLG for the given boundary condition.

(b) Purely mechanical model of multi-layer graphene crinkles

From the DFT analysis presented in §2a, we confirm the existence of a curvature-localizing mode, crinkle, as the lower-energy mode of graphene buckling, pronounced in MLG. The mechanism for formation of crinkle, however, is difficult to completely trace with DFT, as it is computationally very expensive or not possible to simulate larger test cases. To mitigate these limitations and better understand the crinkling process, we formulate a mechanics-based model of a crinkle. To identify the dominant mechanism of crinkle formation, in this section, we first analyse the buckling of elastic layers with weak interlayer-shear coupling without

electromechanical considerations. For the mechanics-based modelling, we follow the notation introduced in figure 1*b*, where we consider *N-layer* MLG, with interlayer spacing $a = 0.34$ nm and total length $2L_0$. The bending stiffness of each layer is denoted as Q_b and the interlayer shear modulus is μ. For the nano-structural model, we make use of DFT-evaluated material properties, $Q_\mathrm{b} = 1.0$ eV [8], and $\mu = 4$ GPa [31]. The continuum plate theories for SLG predict vanishing bending modulus for vanishing thickness. However, the bending energy of SLG originates from relative twisting and rotation of bond angles as well as π-orbital electron cloud shifting, and does not vanish. This energy density is treated as $1/2\, Q_b \kappa^2$ with κ being the curvature. In addition, we use the interatomic distance of the graphene atomic lattice, $c = 0.142$ nm, the in-plane atomic-layer elastic modulus, $Y^{(2D)} = 2000\,\mathrm{eV\,nm^{-2}}$ [32] for dimensional analyses.

The symmetric shape of the crinkle is characterized by the angle $\theta(s)$ that it makes with the horizontal and is parametrized by the arc length s. The entire assembly is under constraint force f to maintain the applied lateral strain. The DFT results indicate that layers deform nearly identically. Since the layers are held together by weak van der Waals forces, we assume translational symmetry in the thickness direction. Owing to the high in-plane stiffness of graphene, the layers are assumed to be inextensible. Under these kinematic assumptions, the strain energy of the system has two contributions, namely the individual-layer bending of the layers and the interlayer shear between them. The energy contribution from these sources is given as

$$U_\mathrm{m} = \int_{-L_0}^{L_0} \left(\frac{Q_b N}{2} \left(\frac{\mathrm{d}\theta}{\mathrm{d}s} \right)^2 + \frac{\mu(N-1)a}{2} \tan^2\theta \right) \mathrm{d}s, \tag{2.1}$$

where the first term represents the bending energy of the layers with the curvature, $\kappa = \mathrm{d}\theta/\mathrm{d}s$, and the second term the interlayer shear energy. The total potential energy of the system is then given as

$$\Pi = U_\mathrm{m} - \int_{-L_0}^{L_0} f(1 - \cos\theta)\, \mathrm{d}s, \tag{2.2}$$

with the last term being the external potential energy of the compressive loading. From the potential energy functional $\Pi(\theta)$ of (2.2) with (2.1), the Euler–Lagrange equation can be readily obtained for the energy minimizing shape $\theta(s)$,

$$Q_b N \theta''(s) - \mu(N-1)a \tan\theta \sec^2\theta + f \sin\theta = 0, \tag{2.3}$$

for $-L_0 \le s \le L_0$, where $(A)'$ denotes $\mathrm{d}A/\mathrm{d}s$. The critical buckling load for end-angles prescribed as $\pm\theta_\mathrm{e}$ at $s = \pm L_0$, predicted by this model is

$$f_\mathrm{cr} = \mu(N-1)a + \frac{\pi^2 Q_b N}{4L_0^2}. \tag{2.4}$$

To give some perspective, we evaluate the critical load for a 100 nm long MLG specimen with 21 layers, and find that bending makes up less than 0.005% of the buckling load. The buckling load is predominantly due to interlayer-shear resistance, and as the length of the layers increases, the bending contribution vanishes.

To carry out the post-buckling analysis, we numerically minimize the potential energy. Figure 2*e* shows the results for one such case with $2L_0 = 100$ nm and 21 layers. For small end angle, the curvature is smoothly distributed over the entire length. As the end angle increases, a progressive symmetric curvature localization occurs. The observed peak curvatures are approximately $0.0067\,\mathrm{nm^{-1}}$ for a 3° end angle, which is much smaller than the DFT predictions in §2b for the same end angles. This discrepancy is attributable to buckling of quantum-flexoelectric dipole–dipole interactions at the nanoscale, which is not accounted for in the purely mechanical model. The quantum flexoelectric effect is treated in depth in §3. In the meantime, to understand the localization behaviour in greater detail, we investigate the band width of curvature focusing given by the two symmetric inflection points of the curvature distribution. For the three cases in figure 2*e*, the band widths of curvature focusing are about 25.1, 12.4 and 10.22 nm in ascending order of the end angles. These band widths are much larger, and change

with the increasing end angle in contrast to DFT results where the band width of curvature focusing is nearly fixed at 0.86 nm. In the limit of very large L_0, two length scales remain in the problem—the interlayer spacing a and another from bending stiffness and interlayer shear, $\sqrt{Q_b/\mu a}$. The EBW of curvature focusing for small θ_e and large L_0 evolves with θ_e as is evident in figure 2*e*. From our numerical study this dependence of EBW is found to be $\sim(\pi/2\theta_e)\sqrt{Q_b/\mu a}$, where the constant $\pi/2$ is introduced to match the best fit curve. Consequently, the curvature focusing observed here is achieved progressively and this mode is not an intrinsic hinge mode of MLG buckling. The curvature localization arises from an energetic competition between bending and interlayer shear energies, where the dominant buckling mechanism is interlayer shear, and bending serves to regularize the localization. Although this purely mechanical model does not completely capture the physics of crinkle formation, it does highlight *one* of the mechanisms of curvature localization in MLG.

(c) Electro-mechanical coupling models of multi-layer graphene crinkles

In §2b we employed a purely mechanical model to study the post-buckling evolution of MLG crinkles and showed that the interplay of interlayer shear and bending energies provides one mechanism of supercritical crinkle formation. Still there are discrepancies between the mechanical model results and DFT predictions. Buckling of MLG creates a strain gradient, i.e. bending curvature of the layers, which breaks the symmetry in the electron cloud distribution in graphene. This separation of positive and negative charge centres in graphene produces a net polarization distribution across the layer. This phenomenon, also known as *quantum flexoelectricity*, is particularly strong in MLG, and a purely mechanical formulation is not able to capture this effect. For a non-piezoelectric flexoelectric material such as graphene, the combined effect of dielectricity and flexoelectricity on polarization, P_i, is given by the following relation,

$$P_i = \alpha_{ij}E_j + \beta_{ijkl}(\nabla\varepsilon)_{jkl}, \tag{2.5}$$

where α_{ij} is the atomic polarizability tensor, E_j is the local electric field component, β_{ijkl} is the flexoelectric tensor and ε is the strain [33].

As discussed in the Introduction, graphene is statically dielectric and flexoelectric in the direction normal to the lattice layer, and (2.5) for graphene is reduced to

$$\check{P} = \alpha\check{E} + \beta_{(N)}\kappa, \tag{2.6}$$

where $\check{P}$ and $\check{E}$ are, respectively, the polarization density and the electric field in the normal direction, while α and $\beta_{(N)}$ are the atomic dielectric polarizability and the intrinsic flexoelectric constant for N layer graphene, respectively. The atomic dielectric polarizability α is given by, $\alpha = \chi/(\chi+1)\epsilon_0 h$, with the electric susceptibility χ, the electric permittivity in vacuum ϵ_0 ($=8.854\times10^{-12}$ F m^{-1}), and the effective dielectric thickness of graphene h, based on the atomic polarization model of [24]. The values of $\chi = 5.9$ and $h = 0.22$ nm were obtained by DFT in [25]. Regarding flexoelectricity, we employ, in this paper, a further simplified model of local coupling between $\check{E}$ and κ, in which the electric field $\check{E}$ induced by layer-bending is effectively proportional to the curvature κ such that

$$\check{P} = \beta^*_{(N)}\kappa, \tag{2.7}$$

where $\beta^*_{(N)}$ is the *effective flexoelectric constant* of N-layer MLG. The highly localized curvature distribution in MLG crinkles allows us to reduce (2.6) to an *effective-locality (e-locality) constitutive relationship* of flexoelectricity. The function $\beta^*_{(N)}/\beta^{(uc)}_{(1)} \cong B_1 - B_2 e^{-B_3 N}$ is obtained by best-fitting a single case ($\theta_e = 3°$) of our e-locality model results to the corresponding DFT results for various N-layered MLGs. The coefficients (B_1, B_2, B_3) are found to be (7.235, 6.841, 0.1377), and the effective flexoelectric constant for a uniform curvature distribution of SLG is given as $\beta^{(uc)}_{(1)} = 0.11e$ by DFT calculation performed in [27].

Electrostatic interactions among the polarized dipoles in the graphene layers provide an energetic contribution to the potential energy. The kinematic assumptions of MLG deformation remain the same as in the purely mechanical model of the previous section. Then, the electrostatic interaction energy is expressed as

$$U_{\text{elec}} = \frac{-\beta^{*2}_{(N)}}{2\pi\epsilon_{(N)}} \sum_{n=1}^{N}\sum_{m=1}^{n} \iint_{-L_0}^{L_0} \kappa(s_n)\kappa(s'_m) \frac{\{1-\delta_{mn}q(s_n,s'_n)\}\{\mathrm{A}(s_n,s'_m)+\mathrm{B}(s_n,s'_m)\}}{[\{x(s_n)-x(s'_m)\}^2+\{y(s_n)-y(s'_m)\}^2]^2}\,\mathrm{d}s_n\,\mathrm{d}s'_m, \tag{2.8}$$

$$A(s_n,s'_m) = \cos\{\theta(s_n)+\theta(s'_m)\}[-\{x(s_n)-x(s'_m)\}^2+\{y(s_n)-y(s'_m)\}^2],$$

$$B(s_n,s'_m) = 2\sin\{\theta(s_n)+\theta(s'_m)\}\cdot\{x(s_n)-x(s'_m)\}\{y(s_n)-y(s'_m)\}$$

$$\text{and } q(s_n,s'_n) = \begin{cases} 1/2 & \text{for } |s_n-s'_n| > r_0 \\ 1, & \text{for } |s_n-s'_n| \le r_0 \end{cases},$$

where r_0 is the cut-off radius of the interaction integration and m, n are indices for the layers for which interactions are considered. Here, $\epsilon_{(N)}$ is the average electric permittivity of N-layered MLG in the normal direction to the layers. Local electric permittivity is layer-position dependent in general [26]; however, we employ the average value for every layer as an approximation for our kinematic assumptions of MLG deformation.

As commonly treated in long-range interactions among singular-field sources, we account for the intralayer dipole–dipole interaction with a cut-off radius. While performing the integration in (2.8), we omit a small symmetric region around the dipole. The way of using cut-off radius to circumvent singularity issues has a physical reasoning behind it. In atomically thin layered materials, the dipoles are not distributed continuously but separated approximately by the lattice parameter distance (nearest neighbours), and thus avoid singularities. Our choice of cut-off radius approximately 0.15 nm is approximately the same as the lattice parameter. Within the cut-off radius, the energy required to uniformly bend graphene is already accounted for in the bending energy, $1/2Q_b\kappa^2$. The bending stiffness value used in the calculations has been obtained from DFT analysis to delineate the bending stiffness from the effect of dipole–dipole interactions.

Augmenting the purely mechanical model with the flexoelectric interaction energy, the total potential energy is formulated as

$$\Pi = \int_{-L_0}^{L_0} \left(\frac{Q_b N}{2}\left(\frac{\mathrm{d}\theta}{\mathrm{d}s}\right)^2 + \frac{\mu(N-1)a}{2}\tan^2\theta - f(1-\cos\theta)\right)\mathrm{d}s + U_{\text{elec}} \tag{2.9}$$

Again, we numerically minimize $\Pi(\theta)$ to get the lowest energy configuration of MLG. Figure 2*f* shows the curvature distributions (refer to the left and bottom axes) for different end angles for a 15 nm long, 21-layered MLG. The curvature distribution is highly localized in an approximately 2 nm band and the peak is much larger compared to the purely mechanical model predictions. The curvature distribution also shows a reversal region, which was absent in the purely mechanical model but predicted by the DFT. Another point of difference between the two models is the boundary layer characterized by the band width of curvature focusing. The e-locality model predicts the 0.86 nm FBW of curvature focusing as shown in figure 2*f* (refer to the right and top axes) in contrast to the EBW exhibited by the purely mechanical sandwich structure model. The much smaller boundary layer is a result of a new length scale in the problem arising from the introduction of flexoelectricity. Once we nondimensionalize (2.9), we have another nondimensionalized quantum-flexoelectric crinkle parameter, $\pi a Q_b\epsilon_{(N)}/\beta^{*2}_{(N)}$, in addition to the purely mechanical crinkle parameter, $(\pi/2a\theta_e)\sqrt{Q_b/\mu a}$, introduced in §2b. Dependence of (2.9) on the quantum-flexoelectric crinkle parameter implies that the energetic competition between flexoelectricity and layer bending yields a band width scaling as $\sim \pi a^2 Q_b\epsilon_{(N)}/\beta^{*2}_{(N)}$, such that higher bending stiffness implies wider band width and higher flexoelectric constant implies narrower width.

3. Analysis of crinkle curvature localization and amplification in graphene

The electromechanical model employing our e-locality constitutive relationship of flexoelectricity, assuming local coupling between $\hat{E}$ and κ, shows all the qualitative features of flexoelectric crinkle as predicted by DFT. In this section, we take a deeper look at the quantitative features of the different models.

(a) Post-buckling characteristics of flexoelectric graphene crinkle

Figure 3*a* shows a comparison of the peak curvature variation versus the kink angle among the DFT, the e-local flexoelectric and the mechanical sandwich structure models. The length of our 21-layer MLG is chosen to be $2L_0 = 15\,\text{nm}$ for both purely-mechanical and flexoelectric models. All three models predict a linear variation of the peak curvature with respect to the kink angle in the post-buckling configuration. Defining the slope of the linear variation as the 'curvature focusing factor', the DFT and the flexoelectric models both predict a curvature focusing factor of approximately $0.05\,2\,\text{nm}^{-1}\,\text{degree}^{-1}$. This is more than 20 times that of the purely mechanical sandwich structure model, approximately $0.0023\,\text{nm}^{-1}\,\text{degree}^{-1}$ shown in figure 2*e*. Thus, the long range dipole–dipole interactions in the flexoelectric layers enhance the curvature focusing more than 20 times. In comparison, the curvature focusing factor for 15 nm long MLG shown in figure 3*a* is approximately $0.004\,\text{nm}^{-1}\,\text{degree}^{-1}$, because the length of the MLG is shorter than the mechanical boundary layer width.

Figure 3*b* exhibits the constraint force normalized by the critical load of pure-shear buckling, 20 µa for our 21-layer MLG model, to keep the end (or kink) angle in the post-buckling configuration, for two different models. One is for the purely mechanical sandwich structure model, the black curve, and the other for the e-local flexoelectric model, the blue curve. These two models match up those of figure 3*a* for $2L_0 = 15\,\text{nm}$. The result of the purely mechanical sandwich structure model corresponds to the constraint force for the interlayer-shear-mode buckling. The interlayer-shear mode of buckling is well known to be supercritical and progressive, and the constraint force versus end angle plot shows a quadratic dependence at the small-angle range. The critical load of the purely mechanical interlayer-shear-mode bifurcation is about 0.53% higher than 20 µa due to finite-length effect of using $2L_0 = 15\,\text{nm}$ specimen. On the other hand, the critical load for flexoelectric crinkle formation (the blue dashed curve in figure 3*b*) is about 0.48% higher than 20 µa, which is lower than the critical load of purely mechanical buckling. The e-local model predicts that with respect to perturbations of complex harmonic modes, the bifurcation is subcritical and the constraint-force should jump to the stable branch of the crinkle post-buckling evolution, shown in blue, in figure 3*b*.

(b) Complex harmonic bifurcation analysis of critical multi-layer graphene buckling

In this sub-section, we perform a linear bifurcation analysis with the e-locality model formulated in §2c. From the full energy expression (2.8), we invoke the linearized small-angle approximation and obtain the following *Euler–Lagrange* equation for the system,

$$Q_b N\theta''(x) + \{f - \mu(N-1)a\}\theta(x) + \frac{\beta^{*2}_{(N)}}{\pi\epsilon_{(N)}}\int_{-L_0}^{L_0}\theta'(\xi)g'_{(N)}(\xi - x)\,\mathrm{d}\xi = 0, \tag{3.1}$$

for $-L_0 \le s \le L_0$, where $g_{(N)}(x-\xi)$ is the dipole–dipole interaction kernel that depends on the number of layers N and the geometry. It excludes $|\xi - x| < r_0$ for intralayer interactions with r_0 the cut-off radius. Now, we look for nontrivial solutions for the above equation for the bifurcation analysis. To this end, we apply the Fourier transformation,

$$\hat{\phi}(k) = \int_{-\infty}^{\infty} \mathrm{e}^{-\mathrm{i}kx}\phi(x)\,\mathrm{d}x, \tag{3.2}$$

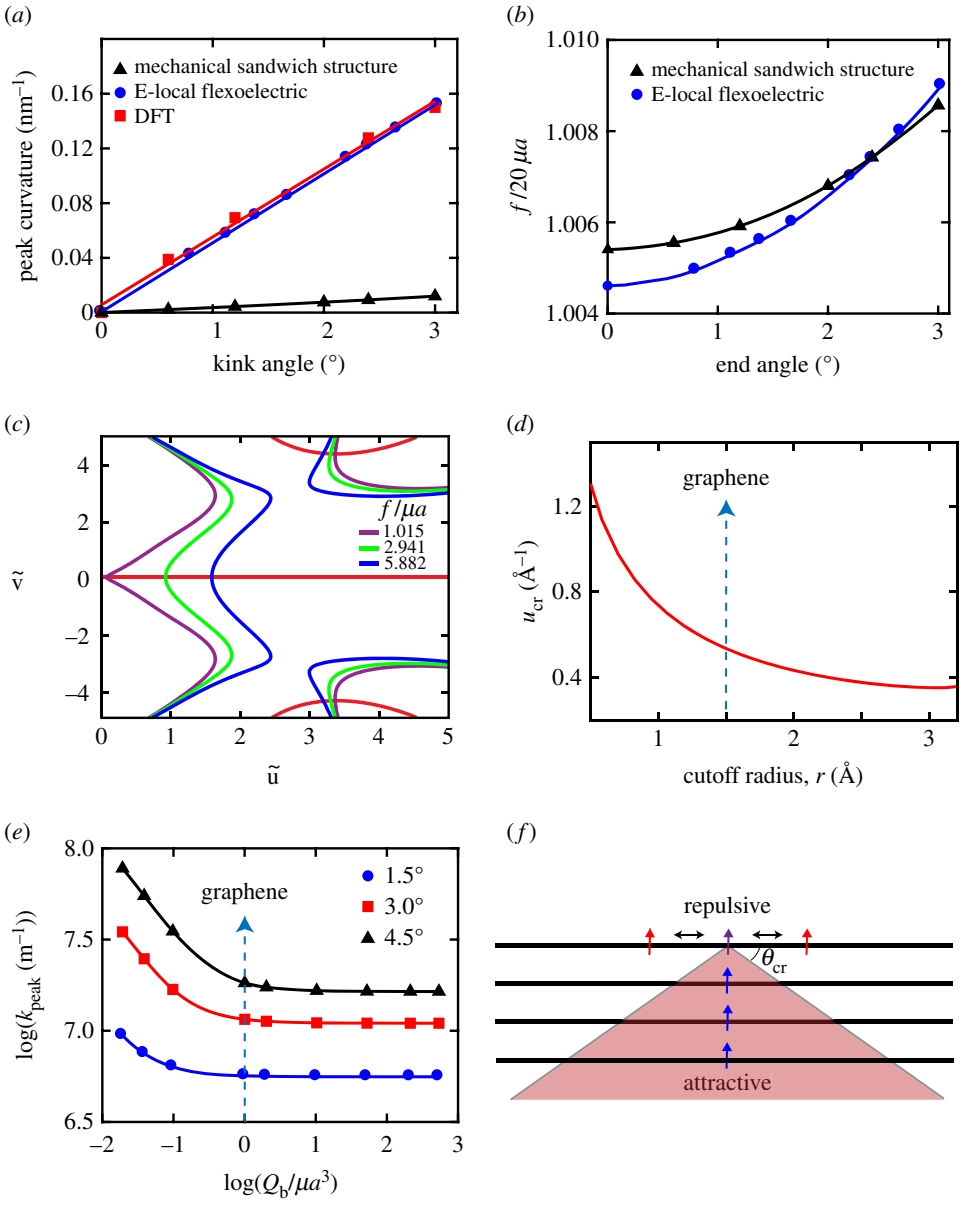

Figure 3. (*a*) Comparison of peak curvature predictions by the purely mechanical model, the e-local flexoelectric model and the DFT as a function of kink angles for 21-layered and 15 nm long MLG; (*b*) Evolution of the constraint force f with end angle for the purely mechanical and the e-local models; (*c*) bifurcation diagram for complex harmonic perturbations from the flat state for a bilayer graphene (red line indicates the solutions for imaginary part, $I_{(2)}(\tilde{u}, \tilde{v}) = 0$, while other colours indicate solutions for real part, $R_{(2)}(\tilde{u}, \tilde{v}; \tilde{f}) = 0$, for different constraint forces.); (*d*) Effect of the cut-off radius r_0 on the critical wavenumber u_{cr} (marker indicates the value used in the analysis for MLG.); (*e*) peak curvature dependence on material properties (this highlights the mechanism of curvature focusing in the purely mechanical model); (*f*) schematic of interlayer and intralayer dipole–dipole interactions in MLG.

to (3.1) with i the unit imaginary number, and obtain,

$$\left\{ f - \mu(N-1)a - k^2 \left(Q_b N - \frac{\beta^{*2}_{(N)}}{\pi \epsilon_{(N)}} \hat{g}_{(N)} \right) \right\} \hat{\theta} = G_{(N)}(\tilde{k}; \tilde{f}) \hat{\theta} = 0, \tag{3.3}$$

where $\hat{\theta}$ is the Fourier transformation of the function $\{\theta(x)$ for $|x| \le L_0$, and $\theta(x) = \theta(L_0)$ for $L_0 < |x|\}$, and $\tilde{k} = ak$ and $\tilde{f} = f/\{(N-1)\mu a\}$ denote non-dimensionalized wavenumber and non-dimensionalized constraint force, respectively. For nontrivial solutions of $\hat{\theta}$, we must satisfy $G_{(N)}(\tilde{k};\tilde{f}) = 0$.

Here, we evaluate the critical complex-harmonic buckling load of a bilayer ($N = 2$) graphene to get physical insight of curvature localization at the onset of bifurcation without loss of generality. For the bilayer model, the kernel $g_{(2)}(\xi - x)$ is given as

$$g_{(2)}(\xi - x) = \frac{-(\xi - x)^2 + a^2}{\{(\xi - x)^2 + a^2\}^2} - \frac{2\{1 - q(\xi, x)\}}{(\xi - x)^2}, \tag{3.4}$$

where the first term comes from interlayer interactions while the second term arises from intralayer interactions. The Fourier transform of $g_{(2)}$, using the definition in (3.2), is calculated to be

$$\hat{g}_{(2)}(k) = \pi |k| e^{-a|k|} + \pi |k| - 2kSi(kr_0) - \frac{2\cos kr_0}{r_0}. \tag{3.5}$$

Complex solutions of $G_{(2)}(\tilde{k};\tilde{f}) = 0$, given by splitting the equation into real and imaginary parts, for $\tilde{k} = \tilde{u} + i\tilde{v}$, yield

$$G_{(2)}(\tilde{k};\tilde{f}) = R_{(2)}(\tilde{u}, \tilde{v};\tilde{f}) + iI_{(2)}(\tilde{u}, \tilde{v}) = 0. \tag{3.6}$$

Equation (3.6) shows that the imaginary-part solution, $I_{(2)}(\tilde{u}, \tilde{v}) = 0$, does not depend on the constraint force, $\tilde{f}$, and is plotted as red curves on the $(\tilde{u}, \tilde{v})$ plane in figure 3*c*, for a bilayer graphene. On the other hand, the real-part solution, $R_{(2)}(\tilde{u}, \tilde{v};\tilde{f}) = 0$, depends on $\tilde{f}$, and is plotted for different values of $\tilde{f}$ with various coloured curves. Intersection points between the red curve and other coloured curves represent the admissible complex wavenumbers corresponding to different values of $\tilde{f}$. The intersection points in figure 3*c* reveal one real ($\tilde{v} = 0$) and two complex conjugate ($\tilde{v} \neq 0$ with same $\tilde{u}$) roots of (3.6).

Since the solution of (3.6) should trace the red curves in figure 3*c*, the red curves represent the fundamental solution branch of bilayer graphene buckling obtained by the complex harmonic analysis. The red line of the real root ($\tilde{v} = 0$) shows the fundamental solution branch for sinusoidal buckling modes. Along this line, admissible buckling modes and corresponding loads are determined by the boundary conditions, similar to the pitchfork bifurcation in Euler column buckling. On the other hand, the complex conjugate roots represent the critical quantum flexoelectric buckling mode, $\theta \sim (A_1 e^{vx} + A_2 e^{-vx}) \sin ux$, at the nanoscale. For a long span ($L_0 \gg a$) of the bilayer graphene, A_1/A_2 vanishes to satisfy the end condition, $\theta \to 0$ at $x = L_0$ for this mode. In figure 3*c*, three complex-conjugate root sets, $(\tilde{u}, \tilde{v}) = (3.385, 4.410), (3.317, 4.426), (3.214, 4.441)$, are displayed for three buckling loads, $\tilde{f} = 1.015, 2.941, 5.882$. The results show that the critical wavenumber and the decay length of the critical quantum flexoelectric buckling mode hardly change with variation of the critical buckling load $\tilde{f}$. However, the critical wave length, approximately 0.63 nm, and the critical decay length, approximately 0.48 nm, for $\tilde{f} \sim 1.015$ are somewhat shorter than those of the post-buckling mode observed in the crinkle ridge boundary layer. It is believed that at the onset of buckling the long-wavelength harmonic mode and the quantum flexoelectric crinkle mode are concurrently activated at the critical load. Then, the critical onset mode jumps to the subcritical post-buckling mode of two straight crinkle wings linked by the curvature focusing boundary layer, adjusting the wavelength and the decay length of curvature distribution. Our parameter study shows that the complex conjugate roots only exist for the quantum flexoelectric crinkle parameter in the range of $1.01 < \pi a Q_b \epsilon_{(2)}/\beta^{*2}_{(2)} < 31.6$. When the value approaches 1.01, the mode becomes harmonic with its wavenumber close to that of the graphene lattice, indicating the trend of spontaneous phase transition from sp_2 to sp_3. On the other hand, when the parameter value exceeds 31.6, the flexoelectric constant is too small to excite the quantum flexoelectric buckling; it can only support the long-wavelength buckling. The bilayer graphene has the value 3.48, indicating that graphene is an ideal material to form quantum flexoelectric crinkles.

(c) Mechanisms of curvature localization in graphene

So far, our energy minimization and bifurcation analyses of the e-local model for flexoelectricity predict the formation of flexoelectric crinkles and the results are in good agreement with the DFT findings. We now take a close look at the energetic interplay that leads to curvature localization in both purely mechanical and electromechanical buckling.

In the purely mechanical model, in the absence of any bending rigidity, a perfectly sharp mathematical kink is the energy minimizing solution that satisfies the boundary conditions. However, with a non-zero bending rigidity, there is an energy competition between interlayer-shear and layer-bending modes. A larger boundary layer allows reduction in the shear energy, which primarily comes from the straight sections of the shape. Thus, we see a smoothly distributed curvature over the length of the sample. However, we would like to point out here that even the purely mechanical model shows non-negligible amount of curvature amplification for small values of $Q_b/\mu a^3$ as shown in figure 3*e*, but for the material properties of graphene, this effect is not significant.

As discussed in the Introduction, long range nonlocal flexoelectric interactions in the model allow for significant energy variations, especially reduction of energy through *attractive* dipole–dipole interactions. The curvature reversal exhibited by the flexoelectric crinkle plays the key role in the energy reduction in the e-local model. Since we employ local coupling in the constitutive relationship, reversal of curvature also implies reversal of polarization. Figure 3*f* shows the schematic of dipole–dipole interactions. There are two types of dipole–dipole interactions—interlayer and intralayer. Interlayer interactions among the dipoles present in the red region are attractive and lower the potential energy. The presence of multiple layers increases the energetic favourability of crinkle formation. Since the crinkle curvature and hence polarization are highly localized, all the interaction is within the shaded (red) region in figure 3*f*.

Intralayer interactions are repulsive for parallel and attractive for anti-parallel dipoles, which is the primary reason why crinkles display the characteristic curvature reversal. The curvature reversal leads to reversal of polarization, and thus the strong attractive intralayer interactions reduce the total energy. This explains the origin of the FBW of curvature focusing. The electrical interaction keeps reducing the potential energy as the boundary layer becomes smaller and smaller. Thus, at the onset of bifurcation there is a spontaneous reduction of boundary layer width which is impeded only by the non-vanishing bending rigidity of graphene. This competition between bending energy and flexoelectric energy gives rise to a boundary layer, substantially smaller than the purely mechanical boundary layer (approx. 2 nm compared to approx. 50 nm). The two mechanisms of curvature focusing work together for flexoelectric crinkles. The energetic competition between layer-bending energy and interlayer-shear energy provides a macroscopic broad-band focusing, while the competition between layer-bending and flexoelectric energy gives a much narrower FBW of curvature focusing and much larger curvature amplification.

4. Discussion

(a) Reduced couplings of flexoelectricity and dielectricity

It is a pleasant surprise that a simple e-local flexoelectric polarization model, (2.7), can capture the major characteristics of critical curvature localization in graphene predicted by DFT analysis. Since $\hat{E}$ in (2.6) is a point-exclusive external electric field, the electric field is generated by all other dipoles distributed in the entire MLG except for the dipole within the cut-off radius, and thus the polarization is inherently nonlocal. However, we lumped the contribution of the nonlocal dielectric interaction term in (2.6) into a single e-local flexoelectric constant $\beta^*_{(N)}$ in (2.7). This lumping for 'uniform curvature distribution' in SLG provides the uc-local polarization constant, $\beta^{(uc)}_{(1)} = 0.11e$, reported in [27]. Similar to electric permittivity, $\epsilon_{(N)}$, the uc-local polarization constant, $\beta^{(uc)}_{(N)}$, is layer-number, N, dependent, and $\beta^{(uc)}_{(21)} \sim 0.718e$, for example. In contrast, a

crinkle has a non-uniform curvature distribution, and we obtain a slightly larger value of the e-local flexoelectric constant, $\beta^*_{(21)} = 0.745e$, by best-fitting the 3°-crinkle curvature distribution predicted by the e-local model to that of the DFT analysis. The value, $\beta^*_{(21)} = 0.745e$, is MLG crinkle specific. In general, the reduced flexoelectric model, from $(\alpha_{(N)}, \beta_{(N)})$ to $(\beta^*_{(N)})$, is not applicable to solve non-uniform curvature problems. However, the peculiar characteristics of the localized curvature distribution, $\kappa(x, \theta_e) = \theta_e \psi(x)$, in the nanoscale MLG crinkle boundary layer allows us to use the reduced effective flexoelectric constant, where $\psi(x)$ is the universal shape function of the crinkle. In the crinkle boundary layer, the antiparallel flexoelectric dipoles in mutually opposite curvature distributions enhance the additional point-exclusive dielectric polarizations. Furthermore, FBW of the boundary layer makes the dielectric polarizations also proportional to the curvature. These two effects make the effective flexoelectric constant $\beta^*_{(21)}$larger than the intrinsic flexoelectric constant, $\beta_{(21)} = 0.726e$. In contrast, flexoelectric dipoles of uniform curvature distribution are parallel to each other and hence the dielectric polarizations are induced in the opposite direction to the flexoelectric dipoles. Therefore, $\beta^{(uc)}_{(N)}$ is smaller than $\beta_{(N)}$. In other words, the net polarization is amplified by dielectricity from the intrinsic flexoelectric polarization in MLG crinkles, and is reduced in uniformly curved MLGs. Although a three-dimensional (3D)-continuum electromechanical constitutive relation in the entire space can be made in a unified manner with thermodynamic representation [34,35], 3D-continuum kinematics cannot effectively follow the deformation of layered structures of inextensible 2D materials. The e-local modelling is found effective in accounting energetics for MLG crinkle deformations. A comparison of the results using $\beta^{(uc)}_{(1)}$ with those using $\beta^*_{(21)}$ is provided in appendix B.

(b) Critical constraint force and the post-buckling mode of multi-layer graphene

For a quantitative assessment of post-buckling behaviour of MLG, we consider the lowest admissible critical load $f_{(2)}$ of sinusoidal interlayer-shear-mode buckling, from (3.3), for a bilayer $(N = 2)$ graphene of length $2L_0 = 15\,\text{nm}$,

$$\tilde{f}_{(2)} = 1 + \frac{k^2}{\mu a}\left(2Q_b - \frac{\beta^{*2}_{(2)}}{\pi\epsilon_{(2)}}\hat{g}_{(2)}\right), \tag{4.1}$$

which evaluates to $\tilde{f}_{(2)} = 1.0164$ for $k = \pi/15\,\text{nm}^{-1}$, $\mu a = 1.36\,\text{N m}^{-1}$, $Q_b = 1\,\text{eV}$, and $\beta^{*2}_{(2)}\hat{g}_{(2)}(k)/\pi\epsilon_0 = -1.175\,\text{eV}$. A negative $\beta^{*2}_{(2)}\hat{g}_{(2)}(k)/\pi\epsilon_0$ implies that the intralayer flexoelectric dipole–dipole interaction of parallel dipoles effectively increase the bending rigidity.

The critical load for the purely mechanical model evaluates to $\tilde{f}_{(2)} = 1.0103$, which is higher than the lowest post-buckling load of crinkle as seen in figure 3*b*. This result indicates that the fundamental state bifurcates at $\tilde{f}_{(2)} = 1.0164$ with a sinusoidal mode which together with the quantum-flexoelectric buckling mode triggers cascading bifurcations of higher orders. These bifurcation events reduce the load to the lowest post-buckling load of crinkle, becoming a subcritical harmonic bifurcation. Once the flexoelectric crinkle is formed at an infinitesimal end angle, subsequent post-buckling load increases with growing end angle, and all the crinkle modes remain identical. The post-buckling mode of the flexoelectric crinkle, $\theta' \sim \sin(k_{(\text{FBW})}x)/x$ within the boundary layer, ensures the characteristics of FBW curvature focusing. If β^* is set to zero, i.e. no flexoelectricity, we recover the purely mechanical supercritical bifurcation and the boundary layer exhibits characteristics of EBW curvature focusing.

A similar phenomenon of subcritical harmonic bifurcation with the invariance of post-bifurcation mode starting at a lower load was previously discovered for the case of creasing in a neo-Hookean solid surface under lateral plane-strain compression [36–39]. For creasing, this mode is singular. The singular crease field was introduced by the cascading subcritical higher-order harmonic bifurcations [18] at the critical compressive strain for harmonic bifurcation [37], called the Biot strain, 0.46 [40]. Alternatively, it could be also introduced by singular perturbation [38] such that the crease initiated at a compressive strain of 0.35, which is smaller than the Biot

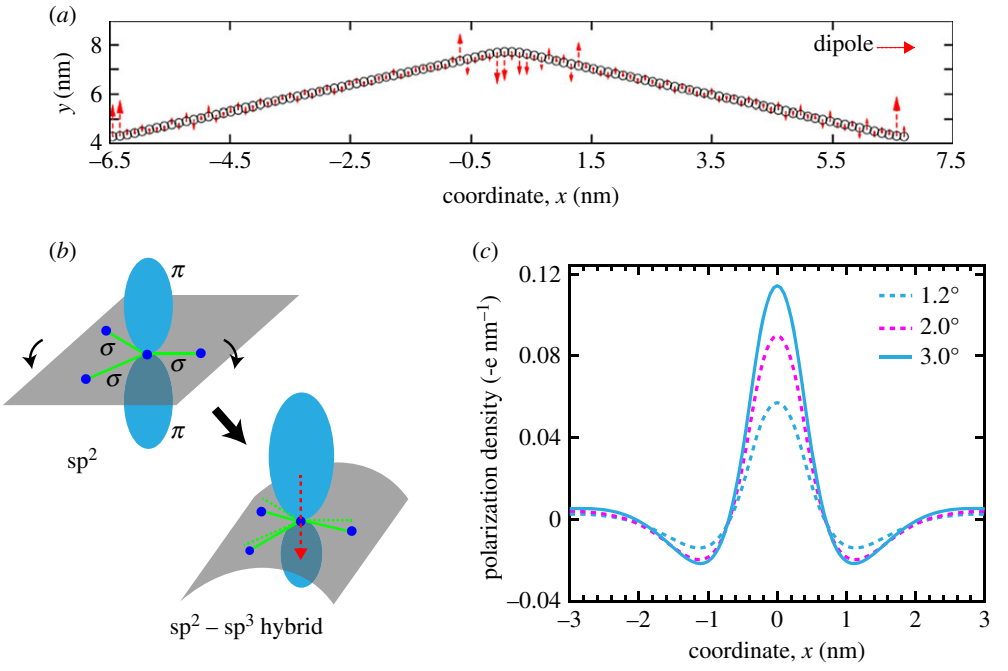

Figure 4. (*a*) Qualitative plot of atomic polarization for a cross section of flexoelectric crinkle from DFT analysis; (*b*) a schematic of electron cloud distortion in bent graphene leading to polarization i.e. quantum flexoelectricity; (*c*) polarization density for 21-layered, 15 nm MLG predicted by e-local model. (Online version in colour.)

strain. For both flexoelectric crinkle and crease cases, the mode grows self-similarly, unlike the progressive growth observed in the supercritical buckling of purely mechanical models.

(c) Crinkle flexoelectric polarization and potential applications

The critical curvature localization in MLG amplifies the peak curvature by two orders of magnitude from that of an equivalent sinusoidal wrinkle to within 0.86 nm FBW for a typical span of the MLG layers, for instance, $2L_0 = 100$ nm in figure 2*e*. For example, the case of a wrinkle with 3° end angle for $2L_0 = 100$ nm has its peak curvature of 0.0016 nm^{-1}, while the equivalent purely mechanical crinkle amplifies this to 0.0068 nm^{-1}, and the flexoelectric crinkle to 0.16 nm^{-1}. The amplification factor is proportional to L_0. An important feature of the MLG crinkle is the development of highly concentrated flexoelectric polarization along the crinkle ridges and valleys. Figure 4*a* shows the DFT-evaluated flexoelectrically polarized dipoles of specific atoms on a cross section of the crinkle. Note the localization and reversal of polarization. As the curvature decays, the polarization also vanishes away from the crinkle ridge. Figure 4*b* highlights the mechanism of intrinsic flexoelectric polarization, where bending leads to π electron cloud shift (in blue) that produces the polarization. The intrinsic flexoelectric polarization further induces additional dielectric polarization. As we obtained in 3.1, the curvature focusing factor for flexoelectric crinkle was 0.052 nm^{-1} $degree^{-1}$, and this large curvature amplification indeed produces a significant net polarization density with peak values reaching 0.12 e nm^{-1} for a 3° kink angle as shown in figure 4*c*.

Curvature localization and amplification lead to development of surface electric-charge concentration in the FBW along the crinkle ridges and valleys on the top and bottom free surfaces of MLG. The surface electric charges are negative on the tops of ridges and positive on the bottoms of valleys. This yields a nanoscale line charge, focused in a 0.86 nm band, and the intensity of the charge concentration can be regulated by controlling the end angle or the level

of compression. We posit that the effects of the crinkle-induced surface line charges have been indirectly observed in literature [41,42]. For instance, DNA molecules are adsorbed along well-ordered lines [41], and C_{60} Buckyballs line up in a regular pattern [40] on HOPG surfaces. We believe that these previously unexplained observations are caused by the presence of flexoelectric line charges resulting from crinkles. HOPG contains naturally existing flexoelectric crinkles along the domain boundaries of the mosaics [7] as discussed in the Introduction. The HOPG crinkle networks are likely generated by inhomogeneous stress fields due to defects introduced during the manufacturing process. DNA molecules are negatively charged, and the DNA molecules are likely adsorbed along the troughs of the crinkle valleys [41]. A straightforward energy minimization calculation accounting for the interactions among the crinkle line charge and the dielectric charges of the Buckyballs shows that the optimal distance between the Buckyballs should be about 2 nm, which is close to the experimentally observed spacing [42]. Typical interaction potential depth between the crinkle line charge and charged molecules or large neutral molecules (or nanoparticles) are much deeper than the Boltzmann activation energy, $k_BT = 25.7$ meV, at room temperature, $T = 298K$. Therefore, we expect that flexoelectric crinkles will be useful in studying self-organizing molecular adsorption for various applications. Besides the potential applications of flexoelectric crinkle charges in adsorption problems, the kinematics and energetics of flexoelectric crinkles can provide new insight on dynamic ripple characteristics in graphene [1]. As DFT analysis reveals that SLG crinkle is a metastable configuration for $2L_0 = 13.26$, the crinkle mode can develop a characteristic phonon mode of ripples in graphene other than the sinusoidal mode, for wavelengths of $4L_0 < 26.5$ nm, and dynamic mode hopping in different modes can play a significant role in thermodynamic energy partitioning and phonon transfer.

5. Conclusion

Here we highlight our new discoveries regarding MLG crinkles:

1. We constructed the MLG phase map of wrinkle versus crinkle. The crinkle phase is more stable than a wrinkle phase for $2L_0 \leq 13.9N\sqrt{(N+1/N)}a$, where $2L_0$, N and a are the whole span, number of layers and the interlayer spacing of a buckling MLG correspondingly.
2. Our DFT analyses reveal that the curvature of the MLG crinkle ridge (or valley) is localized and highly focused within an approximately 0.86 nm wide band. The curvature reaches a peak of approximately 0.15 nm^{-1} for a 3° kink angle, and the curvature vanishes outside of the approximately 2 nm wide boundary layer.
3. We find that a mechanical model of MLG under axial compression undergoes a supercritical interlayer-shear-mode buckling to progressively evolve into a crinkle with its curvature localized within a much broader band than those of DFT predictions. The curvature focusing factor, approximately 0.0023 nm^{-1} $degree^{-1}$, of the purely mechanical model is much weaker than the DFT prediction, approximately 0.052 nm^{-1} $degree^{-1}$. Nevertheless, this long-wavelength mechanical buckling mechanism cooperatively drives MLG crinkle formation with buckling of quantum-flexoelectric dipole–dipole interactions at the nanoscale. The width of the mechanical crinkle is found to be scaled by the mechanical crinkle parameter, $(\pi/2a\theta_e)\sqrt{Q_b/\mu a}$.
4. Our post-buckling analyses of crinkle reveal that long-range non-local electromechanical interactions in MLG promote concurrent quantum flexoelectric buckling of the interactions at the nanoscale, in addition to the long-wavelength purely-mechanical buckling. The attractive interlayer and intralayer interactions among the electric-charge dipoles, generated by flexoelectricity, lower the total potential energy.
5. For an effective crinkle analysis, we formulate an e-local model for graphene flexoelectricity by lumping together the dielectric and flexoelectric interactions in MLG. The e-local model is calibrated with the DFT results to calculate the effective flexoelectric

coefficient $\beta^*_{(21)} = 0.745e$ which is found to be higher than the uc-local polarization constant, $\beta^{(uc)}_{(1)} = 0.11e$, obtained by uniform bending DFT analysis [22].

6. Our e-local model results of flexoelectricity capture the signatures of the crinkles, i.e. curvature focusing, curvature reversal and FBW characteristics observed in the DFT analyses. The peak curvature of $\sim 0.16\,\mathrm{nm}^{-1}$ for 3° end angle and curvature focusing factor of approximately $0.052\,\mathrm{nm}^{-1}\,\mathrm{degree}^{-1}$ are in good agreement with DFT results and are significantly higher than the purely mechanical model.
7. Accounting for flexoelectricity, our linear bifurcation analysis of the e-local model shows that the bifurcation is subcritical with respect to perturbations of complex harmonic modes and happens at a higher critical load of $\tilde{f}_{(2)} = 1.0164$ than the load of purely mechanical model, $\tilde{f}^{\mathrm{mech}}_{(2)} = 1.0103$.
8. Our bifurcation analyses reveal existence of two concurrent hierarchical modes of MLG buckling at the onset of buckling. One is a long-wavelength harmonic bifurcation mode, and the other the quantum flexoelectric crinkle mode near the lattice scale. The two modes at the onset of bifurcation lead to the post-buckling crinkle mode of high curvature localization and focusing at the crinkle ridge (or valley) tips.
9. We have uncovered that the quantum flexoelectric crinkle can be formed only if the quantum flexoelectric crinkle parameter is in the range of $1.01 < \pi a Q_b \epsilon_{(2)}/\beta^{*2} < 31.6$. If the parameter value is close to 1.01, the MLG is likely to make spontaneous phase transition from a sp_2 to a sp_3 structure. On the other hand, if the parameter value is beyond 31.6, the MLG harmonically buckles only with a long wavelength. The quantum flexoelectric crinkle parameter of a bilayer graphene is 3.48, and MLG is found to be an ideal material to form quantum flexoelectric crinkles.
10. The large curvature focusing leads to segregation of charges on the outer surfaces of MLG which are confined within the boundary layer. The polarization density reaches up to $0.12\,\mathrm{e}^-\,\mathrm{nm}^{-1}$ for a 3° kink angle. This effectively produces a line charge, the magnitude of which can be manipulated by macroscopic deformation. Fine control of this class of surface feature with quantum-flexoelectric charge concentration can be a powerful tool to study selective graphene-surface functionalization, molecular adsorption, self-organization of molecular and other nanoscale electrosensitive systems.

Data accessibility. This article has no additional data.

Authors' contributions. M.K. and K.S.K. conceived and implemented the mathematical model, interpreted the results and drafted the manuscript. M.H.C. carried out the DFT analysis. K.S.K. supervised the work. All authors gave final approval for the publication.

Competing interests. We have no competing interests.

Funding. This work was supported by the U.S. National Science Foundation (awards CMMI-1462785 and 1563591) for the experimental study & the theoretical modelling by M.K. and K.S.K., and (awards DMR-0520651 and XSEDE) for the DFT analysis by M.H.C. and K.S.K.

Acknowledgements. Valuable discussions with AK Landauer are gratefully acknowledged.

Appendix A. Phase map analysis of multi-layer graphene

To delineate the different modalities of deformation we construct the phase map as shown in figure 1*d* by comparing the critical load of crinkle versus wrinkle formation for N-layered sandwich structures.

Employing the notation in §2b, the potential energy for the wrinkle mode arising from bending and compression/extension of layers is given as

$$\Pi_{\mathrm{overall}} = N\int_{-L_0}^{L_0} \frac{Q_b}{2}\kappa^2\,\mathrm{d}s + 2\int_{-L_0}^{L_0} \frac{Y^{(2D)}}{2}\left(\sum_{m=1}^{(N-1)/2}\varepsilon_m^2\right)\mathrm{d}s - f\int_{-L_0}^{L_0}(1-\cos\theta)\,\mathrm{d}s, \tag{A 1}$$

where $\varepsilon_m = \pm ma\kappa$ represents the strain in the mth layer away from the central layer by distance ma and N is odd.

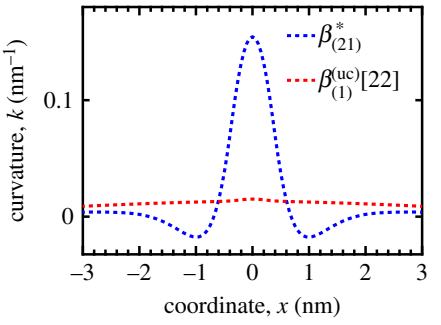

Figure 5. Curvature distributions near a crinkle ridge of 21-layer MLG predicted by 21-layer e-local (blue) and single-layer uc-local (red) flexoelectric models; $2L_0 = 15$ nm. (Online version in colour.)

From (A.1), the critical buckling load for end angles prescribed as $\theta(\pm L_0) = \pm\theta_e$ is calculated to be,

$$f_{\mathrm{cr}}^{(\mathrm{wrinkle})} = \pi^2 \frac{Q_b N}{4L_0^2} + \pi^2 \frac{Y^{(2D)}}{48L_0^2} a^2 N(N^2 - 1). \tag{A 2}$$

Expression of (A 2) is found to be the same for even number of layers.

In contrast to the wrinkling, the critical buckling load for mechanical crinkle, as already discussed in §2b, is given as,

$$f_{\mathrm{cr}}^{(\mathrm{mech.\ crinkle})} = \mu(N-1)a + \frac{\pi^2}{4L_0^2} Q_b N. \tag{A 3}$$

For the mechanical crinkle to be favourable over wrinkle, in the parameter space of L_0 and N, we must have $f_{\mathrm{cr}}^{(\mathrm{mech.\ crinkle})} < f_{\mathrm{cr}}^{(\mathrm{wrinkle})}$. This gives,

$$2L_0 \leq \pi N \sqrt{\frac{Y^{(2D)} a}{12\mu} \left(\frac{N+1}{N}\right)}, \tag{A 4}$$

and for MLG material properties,

$$2L_0 \leq 13.9N \sqrt{\left(\frac{N+1}{N}\right) a}, \tag{A 5}$$

which is the blue curve in figure 1*d*. The asymptotic limit of large N is marked by broken orange curve. The critical load for flexoelectric crinkle formation is found to be even lower than mechanical crinkle formation as discussed in §3. Thus, the phase boundary presented in figure 1*d* is referred to as a lower bound for flexoelectric crinkle formation.

Appendix B. Comparison of e-local and uc-local model predictions

Figure 5 shows the comparison of curvature distribution predicted by the two different models: the uc-local model (red curve) and the e-local model (blue curve). The former uses $\beta_{(1)}^{(\mathrm{uc})} = 0.11e$ obtained from uniform bending DFT study [22] while the latter employs $\beta_{(21)}^{*} \sim 0.745e$ which was obtained by calibrating a single case (3°) to our DFT results for highly non-uniform bending of MLG. The pronounced differences in distribution indicate that $\beta_{(1)}^{(\mathrm{uc})}$ cannot be directly used for non-uniform curvature distribution because non-local coupling effects of dielectricity and electric field become significant.

References

1. Meyer JC, Geim AK, Katsnelson MI, Novoselov KS, Booth TJ, Roth S. 2007 The structure of suspended graphene sheets. *Nature* **446**, 60–63. (doi:10.1038/nature05545)
2. Fasolino A, Los JH, Katsnelson MI. 2007 Intrinsic ripples in graphene. *Nat. Mater.* **6**, 858–861. (doi:10.1038/nmat2011)
3. Landau, LD. 1937 Zur Theorie der Phasenumwandlungen II. *Phys. Z. Sowjetunion* **11**, 26–35.
4. Mermin ND. 1968 Crystalline order in two dimensions. *Phys. Rev.* **176**, 250–254. (doi:10.1103/physrev.176.250)
5. Peierls, R. E. 1935 Quelques proprietes typiques des corpses solides. *Ann. Inst. Henri Poincare* **5**, 177–222.
6. Nelson DR. 1989 Theory of the crumpling transition. In *Statistical mechanics of membranes and surfaces* (eds DR Nelson, T Piran, S Weinberg), pp. 131–148. Singapore, World Scientific.
7. Ohler M, Baruchel J, Moore AW, Galez P, Freund A. 1997 Direct observation of mosaic blocks in highly oriented pyrolytic graphite. *Nucl. Instrum. Methods Phys. Res., Sect. B* **129**, 257–260. (doi:10.1016/s0168-583x(97)00204-8)
8. Jung JH, Bae J, Moon M-W, Kim K-S, Ihm J. 2015 Numerical study on sequential period-doubling bifurcations of graphene wrinkles on a soft substrate. *Solid State Commun.* **222**, 14–17. (doi:10.1016/j.ssc.2015.08.020)
9. Allen HG. 1969 *Analysis and design of sandwich panels*. New York, NY: Pergamon Press.
10. Hunt GW, Silva LSD, Manzocchi GME. 1988 Interactive Buckling in Sandwich Structures. *Proc. R. Soc. Lond. A* **417**, 155–177. (doi:10.1098/rspa.1988.0055)
11. Butz B, Dolle C, Niekiel F, Weber K, Waldmann D, Weber HB, Meyer B, Spiecker E. 2013 Dislocations in bilayer graphene. *Nature* **505**, 533–537. (doi:10.1038/nature12780)
12. Euler, L. 1744 *Methodus inveniendi lineas curvas maximi minimive proprietate gaudentes sive solutio problematis isoperimetrici latissimo sensu accepti*. Lausanne, Switzerland: Marc-Michel Bousquet & Co.
13. Timoshenko SP. 1961 *Theory of elastic stability*. New York, NY: McGraw-Hill Book Company, Inc.
14. Koiter WT. 1945 On the stability of elastic equilibrium (in Dutch with English summary). Thesis, Delft, H.J. Paris, Amsterdam.
15. Budiansky B. 1974 Theory of buckling and post-buckling behavior of elastic structures. *Adv. Appl. Mech.* **14**, 1–65. (doi:10.1016/s0065-2156(08)70030-9)
16. Pipkin AC. 1986 Some examples of crinkles. In *Homogenization and effective moduli of materials and media* (eds JL Ericksen, D Kinderlehrer, R Kohn, J-L Lions), IMA Volumes in Mathematics and its Applications, vol. 1, pp. 182–195. New York, NY: Springer.
17. Diab M, Zhang T, Zhao R, Gao H, Kim K-S. 2013 Ruga mechanics of creasing: from instantaneous to setback creases. *Proc. R. Soc. A* **469**, 20120753. (doi:10.1098/rspa.2012.0753)
18. Diab M, Kim K-S. 2014 Ruga-formation instabilities of a graded stiffness boundary layer in a neo-Hookean solid. *Proc. R. Soc. A* **470**, 20140218. (doi:10.1098/rspa.2014.0218)
19. Zhao R, Zhang T, Diab M, Gao H, Kim K-S. 2015 The primary bilayer ruga-phase diagram I: Localizations in ruga evolution. *Extreme Mech. Lett.* **4**, 76–82. (doi:10.1016/j.eml.2015.04.006)
20. Zhao R, Diab M, Kim K-S. 2016 The primary bilayer ruga-phase diagram II: Irreversibility in ruga evolution. *J. Appl. Mech.* **83**, 91004. (doi:10.1115/1.4033722)
21. Dumitrică T, Landis CM, Yakobson BI. 2002 Curvature-induced polarization in carbon nanoshells. *Chem. Phys. Lett.* **360**, 182–188. (doi:10.1016/s0009-2614(02)00820-5)
22. Kalinin SV, Meunier V. 2008 Electronic flexoelectricity in low-dimensional systems. *Phys. Rev. B* **77**, 033403. (doi:10.1103/physrevb.77.033403)
23. Yudin PV, Tagantsev AK. 2013 Fundamentals of flexoelectricity in solids. *Nanotechnology* **24**, 432001. (doi:10.1088/0957-4484/24/43/432001)
24. Griffiths, David J. 1999 *Introduction to electrodynamics*. Upper Saddle River, NJ: Prentice Hall.
25. Zelisko M, Hanlumyuang Y, Yang S, Liu Y, Lei C, Li J, Ajayan PM, Sharma P. 2014 Anomalous piezoelectricity in two-dimensional graphene nitride nanosheets. *Nat. Commun.* **5**, 4284. (doi:10.1038/ncomms5284)
26. Santos EJG, Kaxiras E. 2013 Electric-field dependence of the effective dielectric constant in graphene. *Nano Lett.* **13**, 898–902. (doi:10.1021/nl303611v)
27. Fang J, Vandenberghe WG, Fischetti MV. 2016 Microscopic dielectric permittivities of graphene nanoribbons and graphene. *Physical Review B* **94**, 045318. (doi:10.1103/physrevb.94.045318)

28. Kresse G, Furthmüller J. 1996 Efficient iterative schemes for ab initio total-energy calculations using a plane-wave basis set. *Phys. Rev. B* **54**, 11 169–11 186. (doi:10.1103/physrevb.54.11169)
29. Kresse G, Joubert D. 1999 From ultrasoft pseudopotentials to the projector augmented-wave method. *Phys. Rev. B* **59**, 1758–1775. (doi:10.1103/physrevb.59.1758)
30. Ihm J, Zunger A, Cohen ML. 1979 Momentum-space formalism for the total energy of solids. *J. Phys. C* **12**, 4409–4422. (doi:10.1088/0022-3719/12/21/009)
31. Shabalin IL. 2014 Carbon (graphene/graphite). In *Ultra-high temperature materials I*, p. 69. Amsterdam, The Netherlands: Springer.
32. Hwang J, Ihm J, Kim K-S, Cha M-H. 2014 Phonon softening and failure of graphene under tensile strain. *Solid State Commun.* **200**, 51–55. (doi:10.1016/j.ssc.2014.09.020)
33. Mindlin RD. 1968 Polarization gradient in elastic dielectrics. *Int. J. Solids Struct.* **4**, 637–642. (doi:10.1016/0020-7683(68)90079-6)
34. Mohammadi P, Liu LP, Sharma P. 2013 A Theory of flexoelectric membranes and effective properties of heterogeneous membranes. *J. Appl. Mech.* **81**, 011007. (doi:10.1115/1.4023978)
35. Liu LP, Sharma P. 2013 Flexoelectricity and thermal fluctuations of lipid bilayer membranes: Renormalization of flexoelectric, dielectric, and elastic properties. *Phys. Rev. E* **87**, 032715. (doi:10.1103/PhysRevE.87.032715)
36. Gent, AN, Cho, IS. 1999 Surface instabilities in compressed or bent rubber blocks. *Rubber Chem.Technol.* **72**, 253–262. (doi:10.5254/1.3538798)
37. Hohlfeld E, Mahadevan L. 2011 Unfolding the Sulcus. *Phys. Rev. Lett.* **106**, 105702. (doi:10.1103/physrevlett.106.105702)
38. Hong W, Zhao X, Suo Z. 2009 Formation of creases on the surfaces of elastomers and gels. *Appl. Phys. Lett.* **95**, 111901. (doi:10.1063/1.3211917)
39. Cao Y, Hutchinson JW. 2011 From wrinkles to creases in elastomers: the instability and imperfection-sensitivity of wrinkling. *Proc. R. Soc. A* **468**, 94–115. (doi:10.1098/rspa.2011.0384)
40. Biot MA. 1963 Surface instability of rubber in compression. *Appl. Sci. Res.* **12A**, 168–182. (doi:10.1007/BF03184638)
41. Liu Z, Zhao L, Zu Y, Tan S, Wang Y, Zhang Y. 2013 Unusual DNA structures formed on bare highly oriented pyrolytic graphite surfaces studied by atomic force Microscopy. *Microsc. Microanal.* **19**, 544–552. (doi:10.1017/S1431927613000275)
42. Klitgaard SK, Egeblad K, Haahr LT, Hansen MK, Hansen D, Svagin J, Christensen CH. 2007 Self-assembly of C60 into highly ordered chain-like structures on HOPG observed at ambient conditions. *Surf. Sci.* **601**, L35–L38. (doi:10.1016/j.susc.2007.03.022)